

Article

Effect of Slag Basicity on Non-Metallic Inclusions and Cleanliness of 15-5PH Stainless Steel

Zhonghua Zhan ¹, Yanling Zhang ^{1,*} , Ruxing Shi ², Tong Qiao ¹, Guanbo Wang ¹ and Guoguang Cheng ¹

¹ State Key Laboratory of Advanced Metallurgy, University of Science and Technology Beijing, Beijing 100083, China

² CITIC Heavy Machinery Co., Ltd., Luoyang 471039, China

* Correspondence: ustbzly1108@163.com; Tel.: +86-010-8237-5191

Abstract: Few reports exist on the effect of the basicity of refining slag on inclusions in 15-5PH stainless steel and its removal efficiency. In this study, the effects of various basicities on the formation and removal efficiency of inclusions in molten steel were investigated. To investigate the effect of the chemical makeup of slag on the non-metallic inclusions in liquid steel, laboratory experiments and thermodynamic calculations were conducted on CaO-MgO-SiO₂-Al₂O₃-CaF₂ slag with various slag basicities and 15-5PH stainless steel. In the steel samples that had reacted with high-basicity slag samples, the magnesium content and aluminum yield were higher. Thermodynamic findings according to the ion and molecule coexistence theory showed that $\log(a_{\text{SiO}_2}^3/a_{\text{Al}_2\text{O}_3}^2)$ decreases as slag basicity increases. This increases the Al concentration in liquid steel while decreasing the Si content. $\log(a_{\text{MgO}}^3/a_{\text{Al}_2\text{O}_3})$ also increases, increasing the Mg content of the molten steel. With this, the transformation order of oxide inclusions is Al₂O₃ → MgAl₂O₄ → MgO. High-basicity slag increases the attachment of slag to inclusions and generates MgAl₂O₄ inclusions that are more easily adsorbed by inclusions in molten steel, thereby improving the cleanliness of molten steel.

Keywords: slag basicity; 15-5PH stainless steel; non-metallic inclusions; cleanliness; work of adhesion



Citation: Zhan, Z.; Zhang, Y.; Shi, R.; Qiao, T.; Wang, G.; Cheng, G. Effect of Slag Basicity on Non-Metallic Inclusions and Cleanliness of 15-5PH Stainless Steel. *Metals* **2023**, *13*, 750. <https://doi.org/10.3390/met13040750>

Academic Editor: Pasquale Cavaliere

Received: 3 March 2023

Revised: 6 April 2023

Accepted: 11 April 2023

Published: 12 April 2023



Copyright: © 2023 by the authors. Licensee MDPI, Basel, Switzerland. This article is an open access article distributed under the terms and conditions of the Creative Commons Attribution (CC BY) license (<https://creativecommons.org/licenses/by/4.0/>).

1. Introduction

As one of the main properties of slag, basicity has a direct effect on the control of O and S content in steel. Research has shown that when slag basicity increases, the total number of inclusions in steel increases and the total area and average radius of the inclusions decrease [1–4]. The proportion of inclusions with a radius less than 2 μm increases significantly, indicating that increasing the basicity of the slag can play a role in refining inclusions. Jiang et al. [5] discovered that, with an increase in slag basicity, the number of Al₂O₃ and brittle inclusions in steel increased and the number of SiO₂ and plastic inclusions decreased. The number of chain inclusions in steel also increases under high-basicity, where the size of point inclusions is large and their number is small; more point inclusions with smaller sizes exist in steel with low basicity, whereas the number of chain inclusions is smaller [6–8]. Li and Yoon et al. [9,10] studied the low-basicity refining slag smelting of high-carbon steel and discovered that in steel acid soluble aluminum [Als] in the range of 0.0005–0.0010%, the Al₂O₃ content of the inclusions in steel was approximately 20%, CaO/Al₂O₃ < 2, and inclusions with good plasticity could be obtained.

Non-metallic impurities must be removed from molten steel via flotation, separation, and dissolution. Initially, inclusions migrate to the steel/slag contact. Subsequently, the surface tension of the steel breaks, stabilizing the inclusions at the steel/slag interface. In the final stage, the inclusion returns to molten steel upon dissolution and is eliminated [11,12]. If the last two steps cannot occur, the inclusions re-enter the molten steel via entrainment, depending on the flow pattern in the ladle or tundish. Previous studies have demonstrated that the separation of solid inclusions occurs extremely rapidly. As per calculations, when a standard slag was added to a secondary refining, the solid inclusions destroyed the

surface tension of the steel within 7–4 s after flotation. This reinforces the discovery of Lee et al. [12,13] in the experimental analysis of solid particles. However, when studying liquid inclusions, up to 7 s was recorded for these inclusions to reach the steel/slag interface. The time difference was caused by the small contact angle between the liquid particles and the molten steel [14–17]. However, the dissolution time of the liquid inclusions was negligible as they were miscible in the slag. Therefore, inclusion removal was the most pronounced for solid inclusions. These inclusions have limited solubility in the slag and are therefore sensitive to the physical and chemical properties, temperature gradient, and volume of the slag [18–21]. Therefore, the removal behavior of solid inclusions is controlled by the mass transfer, reaction kinetics, and chemical interaction with the slag. Thus, dissolution becomes the control step for removing solid inclusions [22–26].

However, few reports exist on the effect of the basicity of refining slag on inclusions in 15-5PH stainless steel and its removal efficiency. In this study, the effects of various basicities on the formation and removal efficiency of inclusions in molten steel were investigated using slag-steel reaction experiments.

2. Experimental Method

Regarding sample preparation, 15-5PH stainless steel was pre-melted in a MgO crucible to fabricate steel sample A. CaO-MgO-SiO₂-Al₂O₃-CaF₂ was pre-melted in a Mo crucible to fabricate slag samples S1, S2, and S3 before reaction with steel. All experiments were conducted under an Ar atmosphere using a vacuum induction furnace. Steel sample A and the pre-melted CaO-MgO-SiO₂-Al₂O₃-CaF₂ slag were balanced in a MgO crucible with a vacuum induction furnace in an Ar atmosphere for 60 min as a preliminary equilibrium experiment. Figure 1 shows a schematic of the experimental setup.

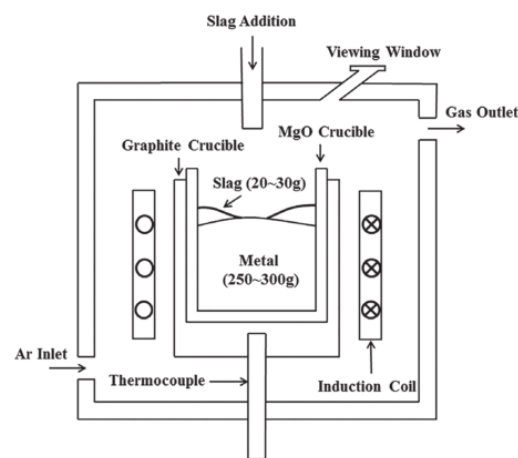


Figure 1. Diagram of the testing equipment.

An amount of 250–300 g of the pre-melted steel was placed in a MgO crucible. The slag/metal reaction chamber was then filled with Ar, followed by induction heating. After the temperature reached 1600 °C, 20–30 g of pre-melted slag was added. The steel and slag samples were removed after the slag was melted at 1600 °C for 60 min. Figure 2 shows a direct observation of the slag/metal reaction process.

The [Si], [Als], [Ca], and [Mg] contents in the steel samples were determined using inductively coupled plasma optical emission spectrometry (ICP-OES) with a relative standard deviation of $\pm 5\%$. The Cr content in the steel samples was determined using the alkali fusion acid dissolution method. The total oxygen content in the steel samples was analyzed using the inert gas melting-infrared absorption method, with an accuracy of ± 1 ppm. The compositions of the slag samples were determined using X-ray fluorescence spectrometry. Tables 1 and 2 show the compositions of the pre-melted steel and slag, respectively. Tables 3 and 4 present the compositions of the steel and slag samples, respectively, after 90 min of the steel slag/metal reaction. The surface of the machined steel sample ($10 \times 10 \times 10$ mm³)

was polished with 240, 400, 800, 1200, and up to 2000 mesh SiC sandpaper. The surface was then ground with a diamond abrasive paste containing a particle diameter of 2.5 μm to determine the size distribution of inclusions in the sample. The characteristics of the inclusions in the steel samples were analyzed using automatic scanning electron microscopy (EVO18-INCAsteel, ZEISS Co., Ltd., Bremen, Germany) combined with scanning electron microscopy W(SEM) and energy-dispersive X-ray spectroscopy (EDS).

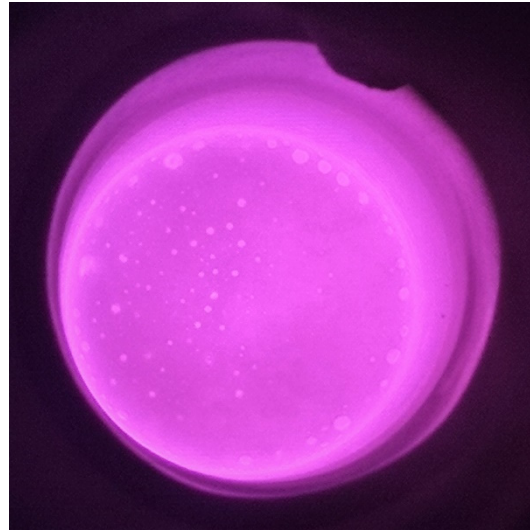


Figure 2. Direct monitoring of the slag/steel interaction.

Table 1. Chemical composition of pre-melted steel Sample A (mass percentage).

Steel	Cr	Ni	Cu	Si	Mn	Mo	C	Nb	O	Mg	Al
A	14.5	5.2	3.0	0.4	0.7	0.3	0.05	0.2	0.0027	0.0002	0.23

Table 2. Chemical composition of premelted slag (Mass percentage).

Slag	CaO	SiO ₂	Al ₂ O ₃	MgO	CaF ₂
S1	46.67	23.33	19.44	5	5
S2	52.50	17.50	19.44	5	5
S3	56.00	14.00	19.44	5	5

Table 3. Chemical composition of the steel samples following the metal/slag reaction (mass percentage).

Steel	Si	Ni	Cr	Cu	Mo	Als	O _{total}	Mg
A1	0.58	5.22	14.84	3	0.34	0.0066	0.002	0.0003
A2	0.57	5.25	14.92	3	0.33	0.014	0.0012	0.0008
A3	0.55	5.26	14.93	3	0.32	0.018	0.0008	0.0012

Table 4. Chemical makeup of the samples of slag following the interaction of slag with metal (mass percentage).

Slag	CaO	SiO ₂	Al ₂ O ₃	MgO	CaF ₂
SA1	40.35	18.11	21.01	15.48	5.05
SA2	48.32	13.59	21.70	11.09	5.30
SA3	50.01	10.80	23.30	11.26	4.64

3. Results and Discussion

3.1. Characterization of Inclusions

Approximately 30 inclusions from each sample collected at various slag compositions were chosen for characterization. Al_2O_3 and a small quantity of Al-Mg-O are the two primary inclusions in Sample A. The elements distribution, EDS spectra, and SEM image of the typical inclusions in Sample A are displayed in Figure 3. The numbers represent the mass percentages discovered during EDS analysis. The Al-Mg-O inclusions exhibit uneven forms, and the majority of the Al_2O_3 inclusions are clusters created by irregular shapes.

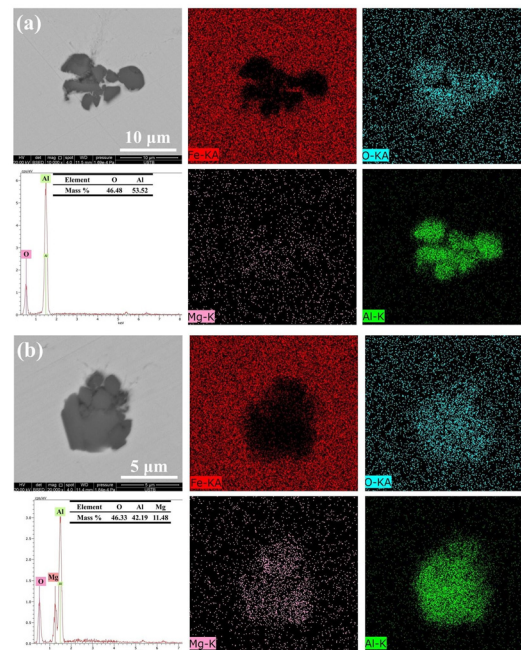


Figure 3. Typical inclusion morphology and makeup of Sample A: (a) Al_2O_3 inclusion; (b) $\text{Al}_2\text{O}_3 \cdot \text{MgO}$ inclusion.

The predominant inclusion in steel sample A1 following a 90-min reaction with slag S1 was Mg-Al-O, as shown in Figure 4a. The majority of inclusions exhibit erratic forms and much smaller sizes. In Figure 4b, the inclusions in samples A and A1 are highlighted to emphasize the development of inclusions in the molten steel. The liquid region (red) of the $\text{MgO-Al}_2\text{O}_3\text{-CaO}$ ternary phase diagram was computed using FactSageTM 8.2 software. The inclusions of Sample A mostly lacked MgO. The 90-min reaction between steel Sample A and slag S1 resulted in a considerable alteration in the steel inclusion makeup. The amount of Al-Mg-O inclusions considerably increased in Sample A1. The Mg level of Sample A1 also increased to 3 ppm (in comparison to 2 ppm for Sample A). Most of the inclusions in Sample A1 had an Al_2O_3 concentration of more than 80%.

The primary inclusions in steel sample A2 were $\text{MgO-Al}_2\text{O}_3$ following a 90-min reaction between steel sample A and slag sample S2. The distribution of the typical $\text{MgO-Al}_2\text{O}_3$ inclusions in Sample A2 is shown in Figure 5a. The inclusions have an irregular polygonal form. The compositions of the inclusions in Samples A and A2 are shown in Figure 5b. The MgO concentration of the majority of the inclusions in Sample A2 grew to more than 60% of the mass after 90 min of the slag/metal reaction. Moreover, Sample A2 had a Mg concentration of up to 8 ppm, which was considerably greater than those of Samples A and A1.

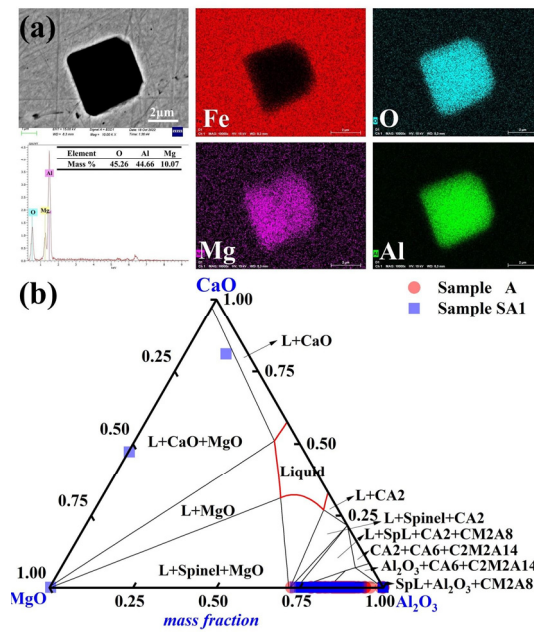


Figure 4. Common inclusions in Sample A1 had the following morphology and composition: (a) elemental distribution of the point inclusions and (b) composition distributions of the inclusions in Samples A and A1 in the MgO-Al₂O₃-CaO phase diagram. At 1600 °C, the solid lines depict the boundaries between several phases.

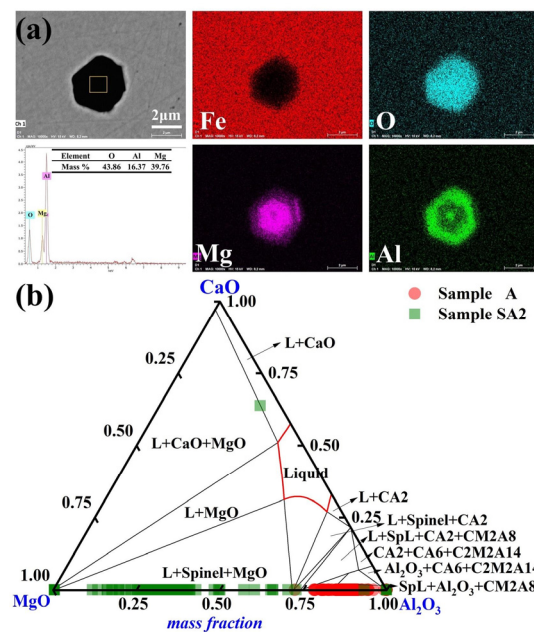


Figure 5. Common inclusions in Sample A2 had the following morphology and composition: (a) elemental distribution of the point inclusions and (b) composition distributions of the inclusions in Samples A and A2 in the MgO-Al₂O₃-CaO phase diagram. At 1600 °C, the solid lines depict the boundaries between several phases.

Pure MgO inclusions became predominant in steel sample A3 following a 90-min reaction with the slag with the highest basicity, S3. The elemental distribution of the typical inclusions in Sample A3 is depicted in Figure 6a. Most inclusions had an amorphous irregular polygonal form. The MgO-Al₂O₃-CaO ternary diagram in Figure 6b highlights the composition of inclusions in Samples A and A3. Compared to the other steel samples,

Sample A3 had a higher Mg concentration of 12 ppm. The features of inclusions in molten steel were considerably influenced by the slag/metal interaction.

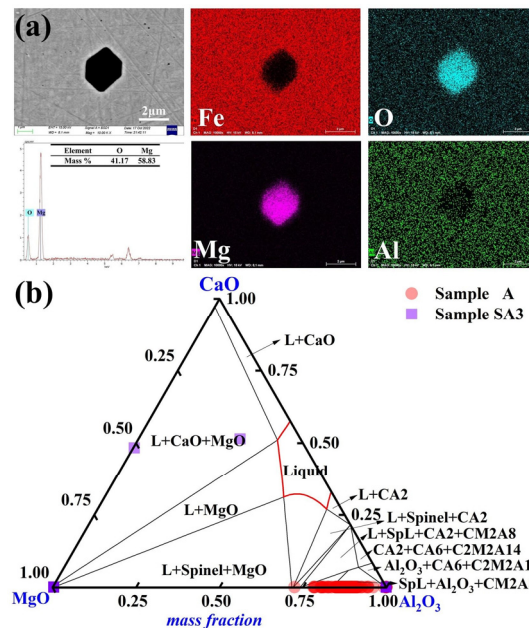


Figure 6. Morphology and makeup of the typical inclusions in Sample A3: (a) elemental distribution of the point inclusions and (b) composition distributions of the inclusions in Samples A and A3 in the MgO-Al₂O₃-CaO phase diagram. At 1600 °C, the solid lines depict the boundaries between several phases.

3.2. Sizes of the Inclusions and Their Densities

Using SEM, EDS, and an automated scanning electron microscope (EVO18-INCAsteel, Zeiss), the shapes and contents of the non-metallic inclusions on the mirror-polished surfaces of the steel specimens were examined. The size of an inclusion was defined as its largest diameter. Because the interaction volume might permeate into the steel and excite electrons from the surroundings of inclusions with a diameter of less than 1 μm , the size was designed to be more than 1 μm .

The size range of inclusions in the three samples, ranging from A to E, is shown in Figure 7. The stainless steel inclusion sizes and number densities in various experimental groups varied considerably. The lowest observed number density of inclusions was found in Experiment C, which involved refining steel with 50.56%, CaO-14.44%, SiO₂-15%, Al₂O₃-10%, and MgO-5% CaF₂ slag. Furthermore, the lowest area percentage of all inclusions was 0.052%. It was also similar to the outcomes of Experiment B. The majority of inclusions in steel were 1–2 μm in size; however, some of them were up to 5 μm . Slag from the refining process may be used more effectively to eliminate bigger particles. The overall number of inclusions in steel decreased from 19.48 mm^{-2} to 11.04, 7.79, and 6.04 mm^{-2} when S1–S3 were refined. Before the response, the area fraction of the total inclusions per unit area decreased from 0.0130% to 0.0077, 0.0054, and 0.0043%. The S3 slag exhibited the lowest inclusion density and area proportion of all inclusions per unit area when compared to the other two refining slags. Therefore, the S3 slag shows the strongest capacity to refine and absorb inclusions. Importantly, a significant correlation existed between the total oxygen concentration and inclusion distribution density in steel. As indicated in Table 3, the total oxygen content of steel decreases with decreasing inclusion distribution density.

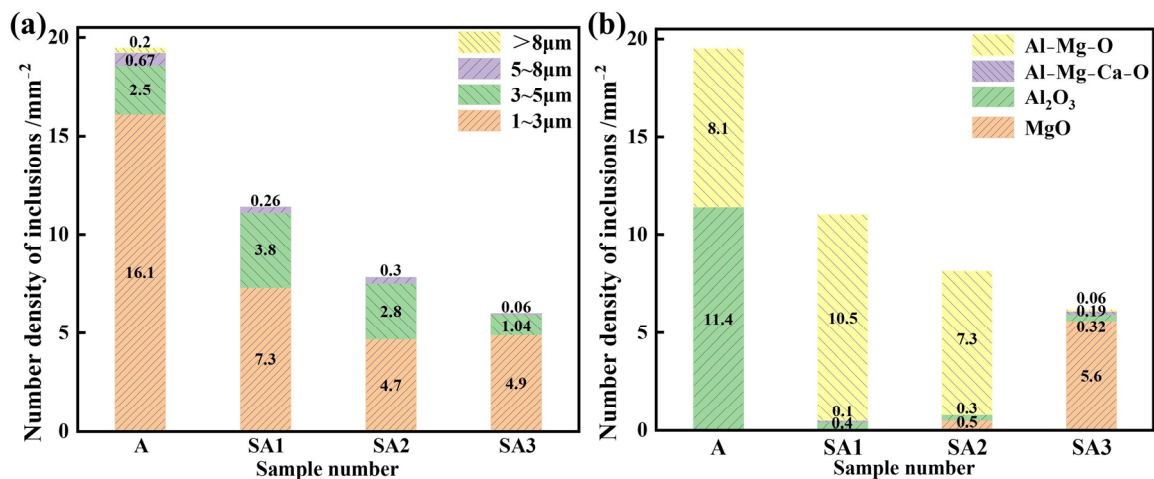


Figure 7. Differences between S1 and S3 in the inclusion number density of the molten steel samples: (a) different inclusion sizes and (b) inclusion types.

The ratio of various inclusion types to the overall inclusion number density is shown in Figure 8. As slag basicity grew, the proportion of MgO inclusions in molten steel increased, the proportion of Al₂O₃ inclusions reduced. In the S1 slag, the proportion of Al-Mg-O inclusions peaked and then decreased. This resulted from changes in the magnesium concentration of molten steel as well as the various adsorption properties of slag on inclusions of Al₂O₃, MgAl₂O₄, and MgO.

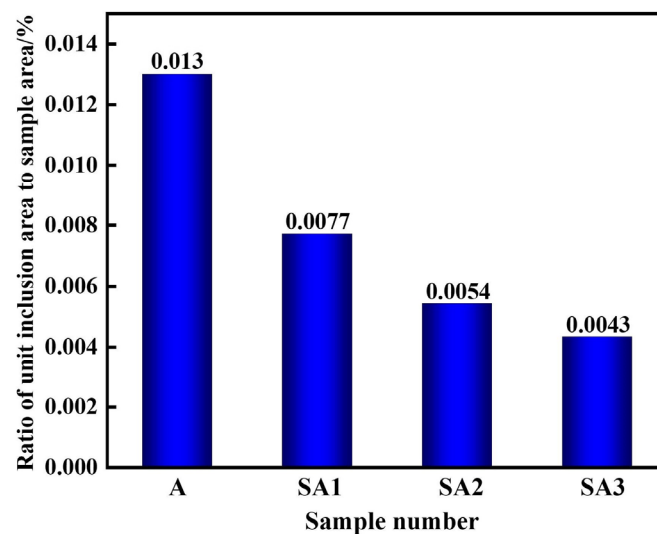


Figure 8. Ratio of unit inclusion area to sample-scanning area in various samples after slag reaction.

Figure 9 shows the difference in chemical composition for various inclusion sizes. Figure 7 shows that the size of the inclusions is distributed in the range of 0–8 µm; therefore, this study focuses on this range. After the interaction of molten steel with slag, Al₂O₃ inclusions gradually changed into Al-Mg-O inclusions, and the MgO concentration of inclusions increased.

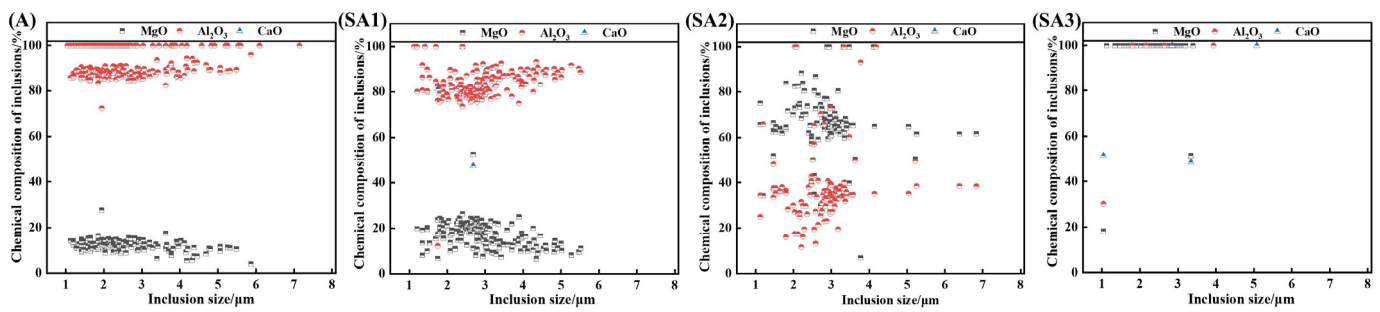


Figure 9. Chemical make-up of the inclusions in samples of steel.

The equilibrium reaction with S1–S3 slags reduced the dissolved oxygen content in molten steel to less than 10×10^{-6} . As shown in Figure 7, various refining slags had different adsorption effects on the Al_2O_3 , MgAl_2O_4 , and MgO inclusions. The slag with the highest alkalinity, S3, had the optimum adsorption capacity for these inclusions. In this study, the adhesion work W was used to evaluate the relative removal effect of refining slag on the Al_2O_3 , MgAl_2O_4 , and MgO inclusions in steel. By measuring the surface tension and contact angle of the molten metal, the adhesion work could be determined, that is, using the Young-Dupré equation [14,27], as shown in Equation (1) [28]:

$$W = \sigma_S(1 + \cos \theta) \quad (1)$$

where W is the adhesion work, σ_S is the surface tension of the refining slag, and θ is the contact angle between slag and substrate. The σ_S value of the slag was obtained using the National Physical Laboratory (NPL) slag model [2], and the slag composition after the reaction is presented in Table 4. The NPL model used to calculate σ_S is founded on the partial molar surface tension of the slag composition, as determined using Equation (2).

$$\sigma_S = X_1\sigma_1 + X_2\sigma_2 + X_3\sigma_3 + X_4\sigma_4 + \dots \quad (2)$$

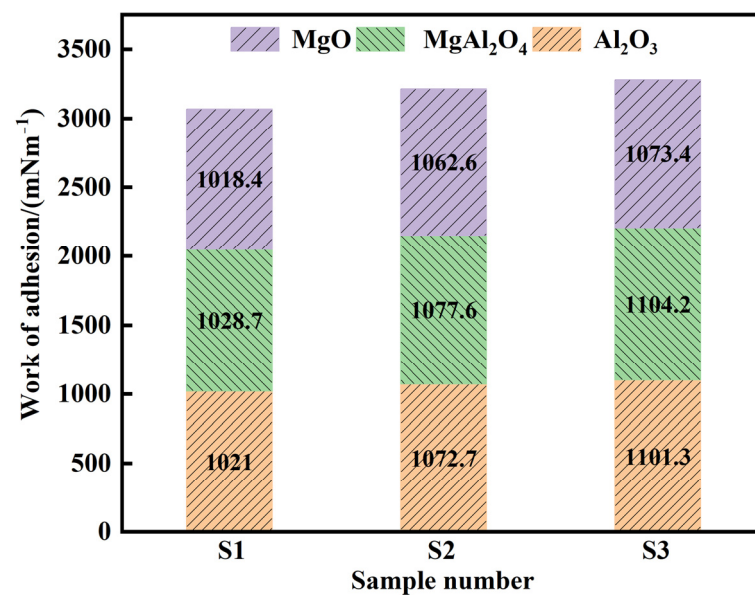
Here σ_i and X_i represent the mole percentage and partial molar surface tension of the slag, respectively. Table 5 presents the surface tensions of each slag component [15,29]. The contact angles between slags of various basicities and the Al_2O_3 , MgAl_2O_4 , and MgO substrates were measured using the test method and are shown in Table 6 [30]. A larger W value indicates stronger bonding between the slag and the Al_2O_3 , MgAl_2O_4 , and MgO inclusions. Figure 10 shows the calculations of the adhesion work between the Al_2O_3 , MgAl_2O_4 , and MgO inclusions in various refining slags. The results show that under the same conditions, the adhesion work of slag S3 to Al_2O_3 , MgAl_2O_4 , and MgO inclusions was the largest at 1101.29, 1104.15, and 1073.41 $\text{mN}\cdot\text{m}^{-1}$, respectively, which is why S3 slag had a better adsorption effect on inclusions (Figure 7). Additionally, the adhesion work showed the trend $W_{\text{MgAl}_2\text{O}_4} > W_{\text{Al}_2\text{O}_3} > W_{\text{MgO}}$ for the inclusions of Al_2O_3 , MgAl_2O_4 , and MgO , and the removal efficiency was the highest in these inclusions.

Table 5. Surface tension of each component in slag systems.

i	Surface Tension $\sigma_i/\times 10^{-3}$ N/m
CaO	625 – 0.094 ($T=1773$)
SiO_2	260 – 0.031 ($T=1773$)
MgO	635 – 0.013 ($T=1773$)
Al_2O_3	655 – 0.177 ($T=1773$)
CaF_2	290 – 0.070 ($T=1773$)

Table 6. Contact angles between various substrates and slags at 1600 °C.

Slag	Substrate	Contact Angle, θ (°)
S1	Alumina	18.26
S2		15.32
S3		11.37
S1	Spinel	11.20
S2		10.40
S3		9.70
S1	Magnesium oxide	11.35
S2		14.60
S3		20.70

**Figure 10.** Adhesion work between the Al₂O₃, MgAl₂O₄, and MgO inclusions in various refining slags.

3.3. Impact of Slag Composition on Molten Steel Inclusions

Duan et al. [31–33] calculated the activity of components in CaF₂-CaO-Al₂O₃-B₂O₃-SiO₂ slag system by IMCT model and FactSage thermodynamic software, respectively. The calculated activity coefficient of B₂O₃ in the slag at 1600 °C is $\gamma_{B_2O_3} = 4.79 \times 10^{-4}$ by employing the IMCT model, which is much higher than that calculated by thermodynamic software. Peng et al. [34] reported that the $\gamma_{B_2O_3} = 2.45 \times 10^{-4}$ in the CaF₂-CaO-Al₂O₃-B₂O₃-SiO₂ slag at 1600 °C using the agglomerated electron phase model. By comparing the activity coefficient of B₂O₃ calculated by different authors, the calculated $\gamma_{B_2O_3}$ by the IMCT model and the agglomerated electron phase model have the same order of magnitude. The value $\gamma_{B_2O_3}$ determined by Peng et al. is slightly lower than the result calculated by the IMCT model, which is likely due to the presence of MgO content reducing the activity coefficient of B₂O₃ in the 1600 °C slag. Duan et al. [35] passed the accuracy of the calculated activity of TiO₂ in the CaF₂-CaO-Al₂O₃-TiO₂(-MgO) slags and that of Ce₂O₃ in the CaF₂-CaO-Al₂O₃-MgO-Ce₂O₃ slag by the IMCT model has been proved by the slag-metal experimental results. Meanwhile, although the calculated activity of B₂O₃ in the CaF₂-CaO-Al₂O₃-B₂O₃-SiO₂ slag by the IMCT model is higher than that by the thermodynamic calculation software at 1600 °C due to the experimental measurement of the activity of B₂O₃ in the slag is rarely reported, the calculated $\gamma_{B_2O_3} = 4.79 \times 10^{-4}$ by the IMCT model at 1600 °C is also testified by the slag-metal experimental results. These results imply that the IMCT model can be reliably applied to calculate the activity of components in slag. Therefore, it is ideal to use IMCT to calculate the slag melt containing CaF₂.

According to Nikolopoulos et al. [36], 21 complex molecules exist in the CaO-CaF₂-MgO-Al₂O₃-SiO₂ slag system. Table 7 shows the expressions for each structural unit, mole number, and mass action concentration in the slag.

Table 7. CaO-MgO-SiO₂-Al₂O₃-CaF₂ slags based on IMCT: expression of structural units as ion couplings or complex molecules, their mole numbers, and mass action concentrations.

Structure Units as Ion Couples or Molecules	Mole Number of Structure Unit	Ion Couples or Structural Unit Mass Action Concentration
Ca ²⁺ + O ²⁻	$n_1 = n_{Ca^{2+}} = n_{O^{2-}}$	$N_1 = 2n_1 / \sum n_i = N_{CaO}$
Ca ²⁺ + 2F ⁻	$n_2 = n_{Ca^{2+}} = 2n_{F^-}$	$N_2 = 3n_2 / \sum n_i = N_{CaF_2}$
Mg ²⁺ + O ²⁻	$n_3 = n_{Mg^{2+}} = n_{O^{2-}}$	$N_3 = 2n_3 / \sum n_i = N_{MgO}$
Al ₂ O ₃	$n_4 = n_{Al_2O_3}$	$N_4 = n_4 / \sum n_i = N_{Al_2O_3}$
SiO ₂	$n_5 = n_{SiO_2}$	$N_5 = n_5 / \sum n_i = N_{SiO_2}$
CaO·SiO ₂	$n_6 = n_{CaO \cdot SiO_2}$	$N_6 = n_6 / \sum n_i = N_{CaO \cdot SiO_2}$
2CaO·SiO ₂	$n_7 = n_{2CaO \cdot SiO_2}$	$N_7 = n_7 / \sum n_i = N_{2CaO \cdot SiO_2}$
3CaO·SiO ₂	$n_8 = n_{3CaO \cdot SiO_2}$	$N_8 = n_8 / \sum n_i = N_{3CaO \cdot SiO_2}$
CaO·Al ₂ O ₃	$n_9 = n_{CaO \cdot Al_2O_3}$	$N_9 = n_9 / \sum n_i = N_{CaO \cdot Al_2O_3}$
CaO·2Al ₂ O ₃	$n_{10} = n_{CaO \cdot 2Al_2O_3}$	$N_{10} = n_{10} / \sum n_i = N_{CaO \cdot 2Al_2O_3}$
CaO·6Al ₂ O ₃	$n_{11} = n_{CaO \cdot 6Al_2O_3}$	$N_{11} = n_{11} / \sum n_i = N_{CaO \cdot 6Al_2O_3}$
3CaO·Al ₂ O ₃	$n_{12} = n_{3CaO \cdot Al_2O_3}$	$N_{12} = n_{12} / \sum n_i = N_{3CaO \cdot Al_2O_3}$
12CaO·7Al ₂ O ₃	$n_{13} = n_{12CaO \cdot 7Al_2O_3}$	$N_{13} = n_{13} / \sum n_i = N_{12CaO \cdot 7Al_2O_3}$
MgO·SiO ₂	$n_{14} = n_{MgO \cdot SiO_2}$	$N_{14} = n_{14} / \sum n_i = N_{MgO \cdot SiO_2}$
2MgO·SiO ₂	$n_{15} = n_{2MgO \cdot SiO_2}$	$N_{15} = n_{15} / \sum n_i = N_{2MgO \cdot SiO_2}$
MgO·Al ₂ O ₃	$n_{16} = n_{MgO \cdot Al_2O_3}$	$N_{16} = n_{16} / \sum n_i = N_{MgO \cdot Al_2O_3}$
3CaO·3Al ₂ O ₃ ·CaF ₂	$n_{17} = n_{3CaO \cdot 3Al_2O_3 \cdot CaF_2}$	$N_{17} = n_{17} / \sum n_i = N_{3CaO \cdot 3Al_2O_3 \cdot CaF_2}$
11CaO·7Al ₂ O ₃ ·CaF ₂	$n_{18} = n_{11CaO \cdot 7Al_2O_3 \cdot CaF_2}$	$N_{18} = n_{18} / \sum n_i = N_{11CaO \cdot 7Al_2O_3 \cdot CaF_2}$
3CaO·2SiO ₂ ·CaF ₂	$n_{19} = n_{3CaO \cdot 2SiO_2 \cdot CaF_2}$	$N_{19} = n_{19} / \sum n_i = N_{3CaO \cdot 2SiO_2 \cdot CaF_2}$
CaO·MgO·SiO ₂	$n_{20} = n_{CaO \cdot MgO \cdot SiO_2}$	$N_{20} = n_{20} / \sum n_i = N_{CaO \cdot MgO \cdot SiO_2}$
CaO·MgO·2SiO ₂	$n_{21} = n_{CaO \cdot MgO \cdot 2SiO_2}$	$N_{21} = n_{21} / \sum n_i = N_{CaO \cdot MgO \cdot 2SiO_2}$
2CaO·MgO·2SiO ₂	$n_{22} = n_{2CaO \cdot MgO \cdot 2SiO_2}$	$N_{22} = n_{22} / \sum n_i = N_{2CaO \cdot MgO \cdot 2SiO_2}$
3CaO·MgO·2SiO ₂	$n_{23} = n_{3CaO \cdot MgO \cdot 2SiO_2}$	$N_{23} = n_{23} / \sum n_i = N_{3CaO \cdot MgO \cdot 2SiO_2}$
2CaO·Al ₂ O ₃ ·SiO ₂	$n_{24} = n_{2CaO \cdot Al_2O_3 \cdot SiO_2}$	$N_{24} = n_{24} / \sum n_i = N_{2CaO \cdot Al_2O_3 \cdot SiO_2}$
CaO·Al ₂ O ₃ ·2SiO ₂	$n_{25} = n_{CaO \cdot Al_2O_3 \cdot 2SiO_2}$	$N_{25} = n_{25} / \sum n_i = N_{CaO \cdot Al_2O_3 \cdot 2SiO_2}$
3Al ₂ O ₃ ·2SiO ₂	$n_{26} = n_{3Al_2O_3 \cdot 2SiO_2}$	$N_{26} = n_{26} / \sum n_i = N_{3Al_2O_3 \cdot 2SiO_2}$

Table 8 displays the reaction equations for the formation of various complex molecules in the slag system, standard Gibbs free energies, and mass action concentration expressions [37,38].

Table 8. Potential complex molecular reaction formulae in CaO-MgO-SiO₂-Al₂O₃-CaF₂ slags.

Reactions	ΔG^θ (J/mol)	N_i
$(Ca^{2+} + O^{2-}) + SiO_2 = CaO \cdot SiO_2$	$-22,476 - 38.52T$	$N_6 = k_1 \cdot N_1 \cdot N_5$
$2(Ca^{2+} + O^{2-}) + SiO_2 = 2CaO \cdot SiO_2$	$-100,986 - 24.03T$	$N_7 = k_2 \cdot N_1^2 \cdot N_5$
$3(Ca^{2+} + O^{2-}) + SiO_2 = 3CaO \cdot SiO_2$	$-93,366 - 23.03T$	$N_8 = k_3 \cdot N_1^3 \cdot N_5$
$(Ca^{2+} + O^{2-}) + Al_2O_3 = CaO \cdot Al_2O_3$	$-18,120 - 18.62T$	$N_9 = k_4 \cdot N_1 \cdot N_4$
$(Ca^{2+} + O^{2-}) + 2Al_2O_3 = CaO \cdot 2Al_2O_3$	$-16,400 - 26.80T$	$N_{10} = k_5 \cdot N_1 \cdot N_4^2$
$(Ca^{2+} + O^{2-}) + 6Al_2O_3 = CaO \cdot 6Al_2O_3$	$-17,430 - 37.20T$	$N_{11} = k_6 \cdot N_1 \cdot N_4^6$
$3(Ca^{2+} + O^{2-}) + Al_2O_3 = 3CaO \cdot Al_2O_3$	$-17,000 - 32.0T$	$N_{12} = k_7 \cdot N_1^3 \cdot N_4$
$12(Ca^{2+} + O^{2-}) + 7Al_2O_3 = 12CaO \cdot 7Al_2O_3$	$-86,100 - 205.1T$	$N_{13} = k_8 \cdot N_1^{12} \cdot N_4^7$
$(Mg^{2+} + O^{2-}) + SiO_2 = MgO \cdot SiO_2$	$43,400 - 40.0T$	$N_{14} = k_9 \cdot N_3 \cdot N_5$
$2(Mg^{2+} + O^{2-}) + SiO_2 = 2MgO \cdot SiO_2$	$-77,403 + 11.0T$	$N_{15} = k_{10} \cdot N_3^2 \cdot N_5$
$(Mg^{2+} + O^{2-}) + Al_2O_3 = MgO \cdot Al_2O_3$	$-35,530 - 2.09T$	$N_{16} = k_{11} \cdot N_3 \cdot N_4$
$3(Ca^{2+} + O^{2-}) + 3Al_2O_3 + (Ca^{2+} + 2F^-) = 3CaO \cdot 3Al_2O_3 \cdot CaF_2$	$-44,492 - 73.15T$	$N_{17} = k_{12} \cdot N_1^3 \cdot N_4^3 \cdot N_2$

Table 8. Cont.

Reactions	ΔG^θ (J/mol)	N_i
$11(\text{Ca}^{2+} + \text{O}^{2-}) + 7\text{Al}_2\text{O}_3 + (\text{Ca}^{2+} + 2\text{F}^-)$ $= 11\text{CaO} \cdot 7\text{Al}_2\text{O}_3 \cdot \text{CaF}_2$	$-228,760 - 155.8T$	$N_{18} = k_{13} \cdot N_1^{11} \cdot N_4^7 \cdot N_2$
$3(\text{Ca}^{2+} + \text{O}^{2-}) + 2\text{SiO}_2 + (\text{Ca}^{2+} + 2\text{F}^-)$ $= 3\text{CaO} \cdot 2\text{SiO}_2 \cdot \text{CaF}_2$	$-255,180 - 8.2T$	$N_{19} = k_{14} \cdot N_1^3 \cdot N_5^3 \cdot N_2$
$(\text{Ca}^{2+} + \text{O}^{2-}) + (\text{Mg}^{2+} + \text{O}^{2-}) + \text{SiO}_2$ $= \text{CaO} \cdot \text{MgO} \cdot \text{SiO}_2$	$-124,766.6 + 3.768T$	$N_{20} = k_{15} \cdot N_1 \cdot N_3 \cdot N_5$
$(\text{Ca}^{2+} + \text{O}^{2-}) + (\text{Mg}^{2+} + \text{O}^{2-}) + 2\text{SiO}_2$ $= \text{CaO} \cdot \text{MgO} \cdot 2\text{SiO}_2$	$-80,387 - 51.916T$	$N_{21} = k_{16} \cdot N_1 \cdot N_3 \cdot N_5^2$
$2(\text{Ca}^{2+} + \text{O}^{2-}) + (\text{Mg}^{2+} + \text{O}^{2-}) + 2\text{SiO}_2$ $= 2\text{CaO} \cdot \text{MgO} \cdot 2\text{SiO}_2$	$-73,688 - 63.639T$	$N_{22} = k_{17} \cdot N_1^2 \cdot N_3 \cdot N_5^2$
$3(\text{Ca}^{2+} + \text{O}^{2-}) + (\text{Mg}^{2+} + \text{O}^{2-}) + 2\text{SiO}_2$ $= 3\text{CaO} \cdot \text{MgO} \cdot 2\text{SiO}_2$	$-315,469 + 24.786T$	$N_{23} = k_{18} \cdot N_1^3 \cdot N_3 \cdot N_5^2$
$2(\text{Ca}^{2+} + \text{O}^{2-}) + \text{Al}_2\text{O}_3 + \text{SiO}_2$ $= 2\text{CaO} \cdot \text{Al}_2\text{O}_3 \cdot \text{SiO}_2$	$-61,964.64 - 60.29T$	$N_{24} = k_{19} \cdot N_1^2 \cdot N_4 \cdot N_5$
$(\text{Ca}^{2+} + \text{O}^{2-}) + \text{Al}_2\text{O}_3 + 2\text{SiO}_2$ $= \text{CaO} \cdot \text{Al}_2\text{O}_3 \cdot 2\text{SiO}_2$	$-13,816.44 - 55.27T$	$N_{25} = k_{20} \cdot N_1 \cdot N_4 \cdot N_5^2$
$3\text{Al}_2\text{O}_3 + 2\text{SiO}_2 = 3\text{Al}_2\text{O}_3 \cdot 2\text{SiO}_2$	$-4354.27 - 10.47T$	$N_{26} = k_{21} \cdot N_4^3 \cdot N_5^2$

According to the law of conservation of mass, the sum of the mass action concentrations of all structural units is 1, which can be expressed according to

$$N_1 + N_2 + \dots + N_{25} + N_{26} = N_1 + N_2 + \dots + k_{20} \cdot N_1 \cdot N_4 \cdot N_5^2 + k_{21} \cdot N_4^3 \cdot N_5^2$$

$$= \sum_{i=1}^{26} N_i = 1 \quad (3)$$

The molar number of the five components in the slag is given by Equations (4)–(8).

$$a_1 = \sum n_i (0.5N_1 + N_6 + 2N_7 + 3N_8 + N_9 + N_{10} + N_{11} + 3N_{12} + 12N_{13} + 3N_{17} + 11N_{18} + 3N_{19} + N_{20} + N_{21} + 2N_{22} + 3N_{23} + 2N_{24} + N_{25})$$

$$= \sum n_i (0.5N_1 + k_1 \cdot N_1 \cdot N_5 + 2k_2 \cdot N_1^2 \cdot N_5 + 3k_3 \cdot N_1^3 \cdot N_5 + k_4 \cdot N_1 \cdot N_4 + k_5 \cdot N_1 \cdot N_4^2 + k_6 \cdot N_1 \cdot N_4^6 + 3k_7 \cdot N_1^3 \cdot N_4 + 12k_8 \cdot N_1^{12} \cdot N_4^7 + 3k_{12} \cdot N_1^3 \cdot N_4^3 \cdot N_2 + 11k_{13} \cdot N_1^{11} \cdot N_4^7 \cdot N_2 + 3k_{14} \cdot N_1^3 \cdot N_5^3 \cdot N_2 + k_{15} \cdot N_1 \cdot N_3 \cdot N_5 + k_{16} \cdot N_1 \cdot N_3 \cdot N_5^2 + 2k_{17} \cdot N_1^2 \cdot N_3 \cdot N_5^2 + 3k_{18} \cdot N_1^3 \cdot N_3 \cdot N_5^2 + 2k_{19} \cdot N_1^2 \cdot N_4 \cdot N_5 + k_{20} \cdot N_1 \cdot N_4 \cdot N_5^2)$$

$$= n_{\text{CaO}} \quad (4)$$

$$a_2 = \sum n_i (1/3N_2 + N_{17} + N_{18} + N_{19})$$

$$= \sum n_i (0.5N_2 + k_{12} \cdot N_1^3 \cdot N_4^3 \cdot N_2 + k_{13} \cdot N_1^{11} \cdot N_4^7 \cdot N_2 + k_{14} \cdot N_1^3 \cdot N_5^3 \cdot N_2)$$

$$= n_{\text{CaF}_2} \quad (5)$$

$$a_3 = \sum n_i (0.5N_3 + N_{14} + 2N_{15} + N_{16} + N_{20} + N_{21} + N_{22} + N_{23})$$

$$= \sum n_i (0.5N_3 + k_9 \cdot N_3 \cdot N_5 + 2k_{10} \cdot N_3^2 \cdot N_5 + k_{11} \cdot N_3 \cdot N_4 + k_{15} \cdot N_1 \cdot N_3 \cdot N_5 + k_{16} \cdot N_1 \cdot N_3 \cdot N_5^2 + k_{17} \cdot N_1^2 \cdot N_3 \cdot N_5^2 + k_{18} \cdot N_1^3 \cdot N_3 \cdot N_5^2)$$

$$= n_{\text{MgO}} \quad (6)$$

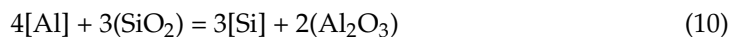
$$\begin{aligned}
 b_1 &= \sum n_i(N_5 + N_6 + N_7 + N_8 + N_{14} + N_{15} + 2N_{19} + N_{20} + 2N_{21} \\
 &\quad + 2N_{22} + 2N_{23} + N_{24} + 2N_{25} + 2N_{26}) \\
 &= \sum n_i(N_5 + k_1 \cdot N_1 \cdot N_5 + k_2 \cdot N_1^2 \cdot N_5 + k_3 \cdot N_1^3 \cdot N_5 + k_9 \cdot N_3 \cdot N_5 \\
 &\quad + k_{10} \cdot N_3^2 \cdot N_5 + 2k_{14} \cdot N_1^3 \cdot N_5^3 \cdot N_2 + k_{15} \cdot N_1 \cdot N_3 \cdot N_5 \\
 &\quad + 2k_{16} \cdot N_1 \cdot N_3 \cdot N_5^2 + 2k_{17} \cdot N_1^2 \cdot N_3 \cdot N_5^2 + 2k_{18} \cdot N_1^3 \cdot N_3 \cdot N_5^2 \\
 &\quad + k_{19} \cdot N_1^2 \cdot N_4 \cdot N_5 + 2k_{20} \cdot N_1 \cdot N_4 \cdot N_5^2 + 2k_{21} \cdot N_4^3 \cdot N_5^2) \\
 &= n_{\text{SiO}_2}
 \end{aligned} \tag{7}$$

$$\begin{aligned}
 b_2 &= \sum n_i(N_4 + N_9 + 2N_{10} + 6N_{11} + N_{12} + 7N_{13} + N_{16} + 3N_{17} + 7N_{18} + N_{24} \\
 &\quad + N_{25} + 3N_{26}) \\
 &= \sum n_i(N_4 + k_4 \cdot N_1 \cdot N_4 + 2k_5 \cdot N_1 \cdot N_4^2 + 6k_6 \cdot N_1 \cdot N_4^6 + k_7 \cdot N_1^3 \cdot N_4 \\
 &\quad + 7k_8 \cdot N_1^{12} \cdot N_4^7 + k_{11} \cdot N_3 \cdot N_4 + 3k_{12} \cdot N_1^3 \cdot N_4^3 \cdot N_2 + 7k_{13} \cdot N_1^{11} \cdot N_4^7 \cdot N_2 \\
 &\quad + k_{19} \cdot N_1^2 \cdot N_4 \cdot N_5 + k_{20} \cdot N_1 \cdot N_4 \cdot N_5^2 + 3k_{21} \cdot N_4^3 \cdot N_5^2) \\
 &= n_{\text{Al}_2\text{O}_3}
 \end{aligned} \tag{8}$$

Based on Equations (3)–(8), the mass action concentration of each component of the slag, that is, the bulk activity, can be obtained using MATLAB R2021b software. The surface phase activity of the slag component satisfies the coexistence theory, that is, the sum of the surface phase activities of all structural units is 1, as demonstrated in Equation (9).

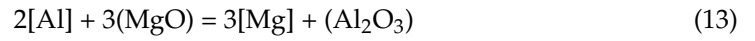
$$\begin{aligned}
 &N_1^{surf} + N_2^{surf} + N_3^{surf} + \dots + N_{25}^{surf} + N_{26}^{surf} \\
 &= N_1^{surf} + N_2^{surf} + N_3^{surf} + \dots + k_{20} \cdot N_1^{surf} \cdot N_4^{surf} \cdot N_5^{surf\ 2} \\
 &\quad + k_{21} \cdot N_4^{surf\ 3} \cdot N_5^{surf\ 2} \\
 &= \sum_{i=1}^{26} N_i^{surf} = 1
 \end{aligned} \tag{9}$$

After adding the deoxidation alloy during the refining of 15-5PH stainless steel, the Al in the molten steel reacts with oxide components in the slag, resulting in the continuous loss of Al via burning. Typically, SiO₂ and MgO in Al-deoxidized stainless steel refining slag react with Al in molten steel, as shown in Equations (10) and (13). These reactions are the main causes of aluminum burning in the molten steel. According to the theoretical model of slag coexistence, N_{SiO_2} , $N_{\text{Al}_2\text{O}_3}$, and N_{MgO} can be used to represent the activities of the slag components a_{SiO_2} , $a_{\text{Al}_2\text{O}_3}$, and a_{MgO} , respectively in Equations (12) and (14). The activity of each component in the slag at 1600 °C was calculated using the coexistence theory of the five-component slag established above. Accordingly, the activity changes of CaF₂, Al₂O₃, and MgO at various slag basicities were calculated, and the results are shown in Figure 11. The calculation results show that with an increase in slag basicity, the activity of the CaF₂ and Al₂O₃ components in the slag gradually decreases, whereas the activity of MgO increases. Furthermore, the variation in $\log(a_{\text{SiO}_2}^3/a_{\text{Al}_2\text{O}_3}^2)$ and $\log(a_{\text{MgO}}^3/a_{\text{Al}_2\text{O}_3})$ with the increase in slag basicity can be extrapolated from Figure 11 (Figure 12). With an increase in slag basicity, $\log(a_{\text{SiO}_2}^3/a_{\text{Al}_2\text{O}_3}^2)$ decreases. According to Equation (12), the decrease in $\log(a_{\text{SiO}_2}^3/a_{\text{Al}_2\text{O}_3}^2)$ results in a higher Si content and lower Al content in molten steel, which increases the burning loss of Al and destroys the “slag-steel” balance, thus affecting the cleanliness of molten steel. With an increase in the slag basicity content, $\log(a_{\text{MgO}}^3/a_{\text{Al}_2\text{O}_3})$ increases. According to Equation (15), an increase in $\log(a_{\text{MgO}}^3/a_{\text{Al}_2\text{O}_3})$ can increase the Mg content in molten steel and lower the Al content. After 90 min of reaction between the molten steel and slag, the experimental findings reveal that the steel sample A1 with the greatest Mg content was obtained from the slag sample SA1 with the lowest slag basicity. The Mg concentration in steel sample A1 reached 12 ppm at this point.



$$K_1 = \frac{a_{\text{Si}}^3 \cdot a_{\text{Al}_2\text{O}_3}^2}{a_{\text{Al}}^4 \cdot a_{\text{SiO}_2}^3} \tag{11}$$

$$\log \frac{a_{\text{Si}}^3}{a_{\text{Al}}^4} = \log \frac{a_{\text{SiO}_2}^3}{a_{\text{Al}_2\text{O}_3}^2} + \log K_1 \tag{12}$$



$$K_2 = \frac{a_{\text{Mg}}^3 \cdot a_{\text{Al}_2\text{O}_3}}{a_{\text{Al}}^2 \cdot a_{\text{MgO}}^3} \tag{14}$$

$$\log \frac{a_{\text{Mg}}^3}{a_{\text{Al}}^2} = \log \frac{a_{\text{MgO}}^3}{a_{\text{Al}_2\text{O}_3}} + \log K_2 \tag{15}$$

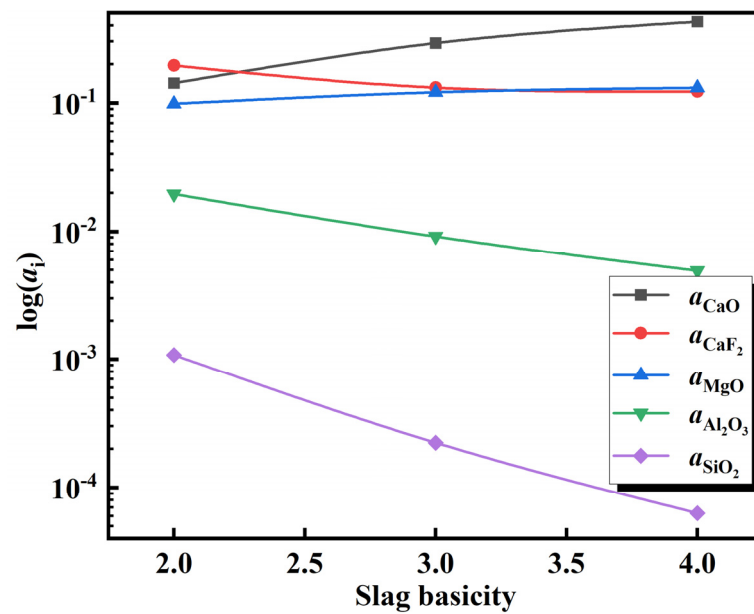


Figure 11. Relationship of activity with slag basicity.

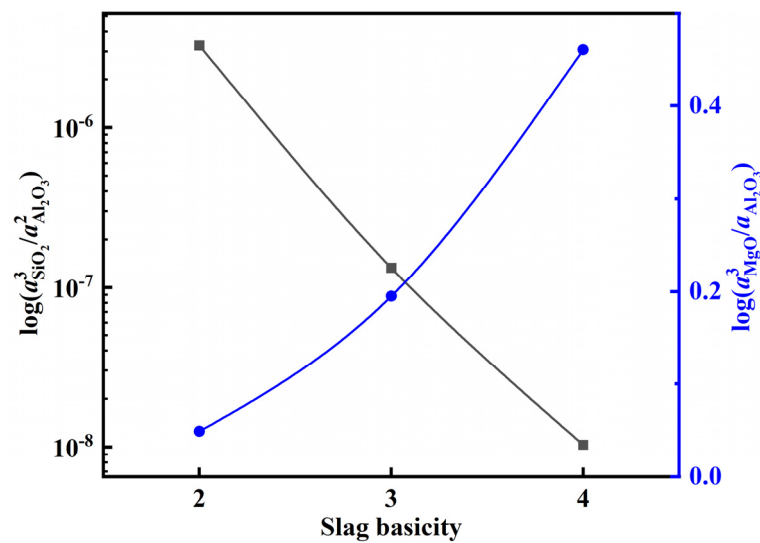


Figure 12. Dependence of $\log(a_{\text{SiO}_2}^3/a_{\text{Al}_2\text{O}_3}^2)$ and $\log(a_{\text{MgO}}^3/a_{\text{Al}_2\text{O}_3})$ on slag basicity.

The production of inclusions in steel is substantially affected by the increase in the Mg concentration in molten steel. Using FactSage™ 8.2 software, the Al-Mg stable phase diagram of 15-5PH stainless steel at 1600 °C was predicted (Figure 13). The transition sequence of oxide inclusions changed from Al₂O₃ → MgAl₂O₄ → MgO when the Mg level in molten steel increased from 2 to 12 ppm. Figure 13 shows the Mg content of the experimental steel samples. The composition of Samples A1 and A2 was in the spinel phase, whereas the composition of Sample A3 was in the MgO phase, as shown in Figure 13. The experimental results were in strong agreement with the calculated results.

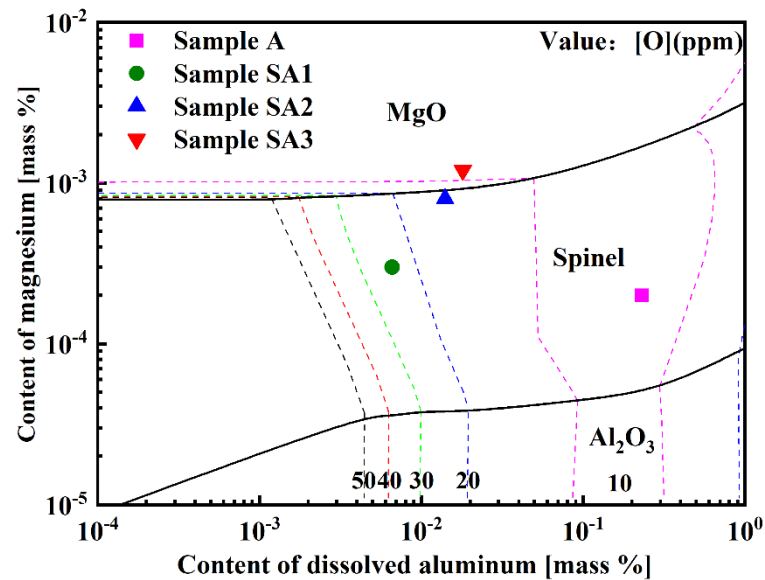


Figure 13. Al-Mg stable phase diagram of 15-5PH stainless steel at 1600 °C.

3.4. Evolution Mechanism of the Inclusions in Steel

Figure 14 depicts the evolution mechanism of the reaction between oxide inclusions in 15-5PH stainless steel and CaO-MgO-SiO₂-Al₂O₃-CaF₂ slag with various basicities. This mechanism was determined via experimental findings and thermodynamic analysis.

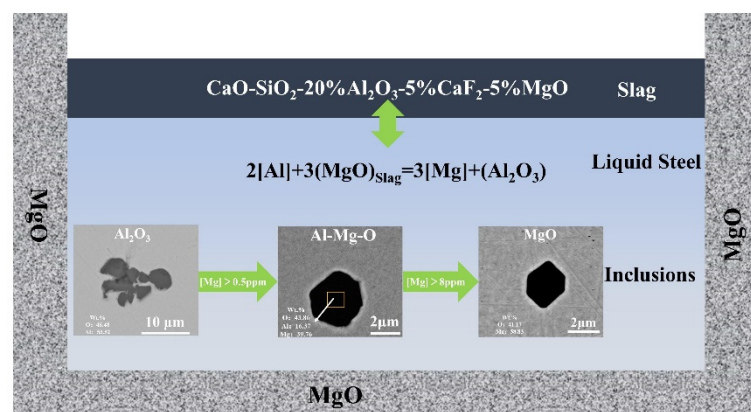


Figure 14. The CaO-MgO-SiO₂-Al₂O₃-CaF₂ slag and inclusion reaction evolution mechanism in 15-5PH stainless steel.

The basicity of the slag affects the Al and Si contents in the molten steel. According to thermodynamic analysis, an extremely low basicity increases the Si content in molten steel as the increase in slag basicity reduces $\log(a_{\text{SiO}_2}^3/a_{\text{Al}_2\text{O}_3}^2)$ in the slag. The experimental results showed that the Si concentration in the lowest basicity steel, Sample A1, is 0.58%, which is consistent with the thermodynamic analysis. Furthermore, the Si content in the

molten steel is the highest among all the samples, which reduces the purity of the molten steel and increases the loss of aluminum via burning.

The composition of the inclusions in molten steel is considerably influenced by the slag basicity. With an increase in slag basicity, $\log(a_{\text{MgO}}^3/a_{\text{Al}_2\text{O}_3})$ increases; therefore, the Mg content in molten steel increases. The Mg content of the steel sample reacting with the high-basicity slag was higher, which agrees with the thermodynamic analysis. The development of MgO-Al₂O₃ inclusions in molten steel was shown to be influenced by Mg concentration, according to thermodynamic calculations. With an increase in the Mg content in the molten steel, the spinel phase (MgAl₂O₄) inclusions transformed into the MgO phase, increasing the MgO content in the inclusions. This is consistent with the results of Li et al. [33]. When the slag basicity increased from 2 in Sample S1 to 4 in Sample S3, the Mg content in the molten steel increased from 3 ppm in Sample A1 to 12 ppm in Sample A3. All inclusions in the steel changed to MgO. After the slag/metal reaction, the increase in the slag basicity causes an increase in the Mg content in the molten steel, which increases the MgO content in the inclusions in the steel until they are completely converted to MgO.

4. Conclusions

In this investigation, the slag/metal reaction at 1600 °C was used to examine the influence of the CaO-MgO-SiO₂-Al₂O₃-CaF₂ slag composition on the development of inclusions in 15-5PH stainless steel. The following conclusions were reached based on the experimental findings and thermodynamic analysis:

(1) The Si concentration is greater in the samples of slag steel with the lowest basicity. According to the thermodynamic findings based on IMCT, an increase in slag basicity lowers $\log(a_{\text{SiO}_2}^3/a_{\text{Al}_2\text{O}_3}^2)$ in the slag, increasing the Al yield of the steel. Si concentration is highest in steel Sample A3, which has the lowest basicity slag.

(2) The Mg content in molten steel is significantly affected by slag basicity. With an increase in slag basicity, $\log(a_{\text{MgO}}^3/a_{\text{Al}_2\text{O}_3})$ decreases, and the Mg content in molten steel increases. Steel sample A3, with a slag basicity of 4 had a Mg content of 12 ppm, which was significantly higher than the A1 steel sample with a slag basicity of 2. As the content of Mg in the steel increases, the transitional order of oxide clamps is Al₂O₃ → MgAl₂O₄ → MgO.

(3) The order of the adhesion work of inclusions in molten steel is $W_{\text{MgAl}_2\text{O}_4} > W_{\text{Al}_2\text{O}_3} > W_{\text{MgO}}$. The increase in slag basicity increases the adhesion work of slag to inclusions and forms inclusion types that are easier to remove, thus increasing the purity of molten steel.

Author Contributions: Conceptualization and writing, Z.Z.; original draft preparation, Z.Z. and Y.Z.; methodology and formal analysis, Z.Z., T.Q., G.W., Y.Z., R.S. and G.C.; validation and formal analysis, Z.Z., Y.Z. and G.C.; supervision, Z.Z. and Y.Z. All authors have read and agreed to the published version of the manuscript.

Funding: This study was supported by the National Natural Science Foundation of China (U1960201) and the National Key R&D Program of China (2019YFC1905701).

Data Availability Statement: Not applicable.

Conflicts of Interest: The authors declare no conflict of interest.

References

1. Zhang, H.; Peng, Y.; Zhang, S.; Liu, C.; Cheng, R.; Ni, H. Effects of refining slag on transformation and removal of inclusions in type 430 stainless steel. *Met. Mater. Trans. B* **2022**, *53*, 702–715. [CrossRef]
2. Peng, Y.; Liu, C.; Yang, L.; Hou, S.; Cheng, R.; Zhang, H.; Ni, H. Improving cleanliness of 30Cr2Ni4MoV low-pressure rotor steel by CaO-SiO₂-MgO-Al₂O₃ slag refining. *J. Iron Steel Res.* **2022**, *29*, 1434–1445. [CrossRef]
3. Sasai, K. Kinetics on formation, growth and removal of alumina inclusions in molten steel. *Tetsu-to-Hagane* **2021**, *107*, 785–795. [CrossRef]
4. Jiang, M.; Li, K.; Wang, R.; Yang, E.; Wang, X. Cleanliness and control of inclusions in Al-deoxidized bearing steel refined by basic slags during LF-VD-Ar Bubbling. *ISIJ Int.* **2021**, *62*, 124–132. [CrossRef]
5. Jiang, M.; Wang, X.; Chen, B.; Wang, W. Formation of MgO-Al₂O₃ inclusions in high strength alloyed structural steel refined by CaO-SiO₂-Al₂O₃-MgO Slag. *ISIJ Int.* **2008**, *48*, 885–890. [CrossRef]

6. Park, J.H.; Kang, Y. Inclusions in stainless steels—A review. *Steel Res. Int.* **2017**, *88*, 1700130. [[CrossRef](#)]
7. Park, J.S.; Park, J.H. Effect of physicochemical properties of slag and flux on the removal rate of oxide inclusion from molten steel. *Met. Mater. Trans. B* **2016**, *47*, 3225–3230. [[CrossRef](#)]
8. Hu, Y.; Chen, W. Influence of refining slag composition on cleanliness and fatigue life of 60Si2MnA spring steel. *Ironmak. Steelmak.* **2016**, *43*, 340–350. [[CrossRef](#)]
9. Li, M. *Study on Cleanliness of Shougang Cord Steel*; University of Science and Technology Beijing: Beijing, China, 2006.
10. Yoon, B.; Heo, K.; Kim, J. Improvement of steel cleanliness by controlling slag composition. *Ironmak. Steelmak.* **2002**, *29*, 215–218. [[CrossRef](#)]
11. Park, J.H.; Jung, I.H.; Lee, H.G. Dissolution behavior of Al₂O₃ and MgO inclusions in the CaO–Al₂O₃–SiO₂ slags: Formation of ring-like structure of MgAl₂O₄ and Ca₂SiO₄ around MgO inclusions. *ISIJ Int.* **2006**, *46*, 1626–1634. [[CrossRef](#)]
12. Valdez, M.; Shannon, G.S.; Sridhar, S. The ability of slags to absorb solid oxide inclusions. *ISIJ Int.* **2006**, *46*, 450–457. [[CrossRef](#)]
13. Lee, S.; Tse, C.; Yi, K.W.; Misra, P.; Chevrier, V.; Orrling, C.; Sridhar, S.; Cramb, A.W. Separation and dissolution of Al₂O₃ inclusions at slag/metal interfaces. *J. Non-Cryst. Solids* **2001**, *282*, 41–48. [[CrossRef](#)]
14. Ni, P.; Goto, H.; Nakamoto, M.; Tanaka, T. Neural network modelling on contact angles of liquid metals and oxide ceramics. *ISIJ Int.* **2020**, *60*, 1586–1595. [[CrossRef](#)]
15. Mills, K.; Karagadde, S.; Lee, P.; Yuan, L.; Shahbazian, F. Calculation of physical properties for use in models of continuous casting process-Part 1: Mould slags. *ISIJ Int.* **2016**, *56*, 264–273. [[CrossRef](#)]
16. Abdeyazdan, H.; Dogan, N.; Rhamdhani, M.; Chapman, M.; Monaghan, B. Dynamic wetting of CaO–Al₂O₃–SiO₂–MgO liquid oxide on MgAl₂O₄ spinel. *Met. Mater. Trans. B* **2014**, *46*, 208–219. [[CrossRef](#)]
17. Furukawa, T.; Saito, N.; Nakashima, K. Evaluation of interfacial energy between molten Fe and Fe-18%Cr-9%Ni alloy and non-metallic inclusion-type oxides. *ISIJ Int.* **2021**, *61*, 2381–2390. [[CrossRef](#)]
18. Reis, B.H.; Bielefeldt, W.V.; Vilela, A.C.F. Absorption of non-metallic inclusions by steelmaking slags—A review. *J. Mater. Res. Technol.* **2014**, *3*, 179–185. [[CrossRef](#)]
19. Todoroki, H.; Mizuno, K. Effect of silica in slag on inclusion compositions in 304 stainless steel deoxidized with aluminum. *ISIJ Int.* **2004**, *44*, 1350–1357. [[CrossRef](#)]
20. Monaghan, B.; Chen, L.; Sorbe, J. Comparative study of oxide inclusion dissolution in CaO–SiO₂–Al₂O₃ slag. *Ironmak. Steelmak.* **2013**, *32*, 258–264. [[CrossRef](#)]
21. Ma, W.; Bao, Y.; Wang, M.; Zhao, D. Influence of slag composition on bearing steel cleanliness. *Ironmak. Steelmak.* **2013**, *41*, 26–30. [[CrossRef](#)]
22. Rocha, V.; Pereira, J.; Yoshioka, A.; Bielefeldt, W.; Vilela, A. Evaluation of secondary steelmaking slags and their relation with steel cleanliness. *Met. Mater. Trans. B* **2017**, *48*, 1423–1432. [[CrossRef](#)]
23. He, X.; Wang, X.; Chen, S.; Jiang, M.; Huang, F.; Wang, W. Inclusion composition control in tyre cord steel by top slag refining. *Ironmak. Steelmak.* **2014**, *41*, 676–684. [[CrossRef](#)]
24. Li, X.; Wang, L.; Yang, S.; Zhuang, C. Effect of slag composition on the cleanliness of drill rod steel. *Ironmak. Steelmak.* **2018**, *46*, 416–423. [[CrossRef](#)]
25. Liu, C.; Gao, X.; Ueda, S.; Kitamura, S. Change in composition of inclusions through the reaction between Al-killed Steel and the slag of CaO and MgO saturation. *ISIJ Int.* **2019**, *59*, 268–276. [[CrossRef](#)]
26. Mu, H.; Zhang, T.; Fruehan, R.; Weblar, B. Reduction of CaO and MgO slag components by Al in Liquid Fe. *Met. Mater. Trans. B* **2018**, *49*, 1665–1674. [[CrossRef](#)]
27. Yang, G.; Wang, X.; Huang, F.; Wang, W.; Yin, Y. Transient inclusion evolution during RH Degassing. *Steel Res. Int.* **2014**, *85*, 26–34. [[CrossRef](#)]
28. Nakajima, K. Estimation of surface tension for multicomponent silicate Melts. *Tetsu-to-Hagane* **1994**, *80*, 599–604. [[CrossRef](#)]
29. Nakajima, K. Estimation of interfacial tensions between phases in the molten iron-slag-inclusion (Alumina) system. *Tetsu-to-Hagane* **1994**, *80*, 383–388. [[CrossRef](#)]
30. Gao, M.; Yu, H.; Cheng, G.; Zhang, Y. Experimental study on high temperature wetting behavior of molten metal/slag-oxide. *Exp. Technol. Manag.* **2022**, *39*, 5–11.
31. Duan, S.; Lee, M.; Kim, D.; Park, J. Oxidation behavior of boron in 9CrMoCoB steel by CaF₂–CaO–Al₂O₃–SiO₂–B₂O₃ electroslag remelting (ESR) type slag. *J. Mater. Res. Technol.* **2022**, *17*, 574–585. [[CrossRef](#)]
32. Zhang, J.; Wang, P. The widespread applicability of the mass action law to metallurgical melts and organic solutions. *Calphad* **2001**, *25*, 343–354. [[CrossRef](#)]
33. Jiang, Z.; Hou, D.; Dong, Y.; Cao, Y.; Cao, H.; Gong, W. Effect of Slag on Titanium, Silicon, and Aluminum Contents in Superalloy During Electroslag Remelting. *Met. Mater. Trans. B* **2016**, *47*, 1465–1474. [[CrossRef](#)]
34. Peng, L.; Jiang, Z.; Geng, X. Design of ESR slag for Remelting 9CrMoCoB steel through experiments and thermodynamic calculations. *Calphad* **2020**, *70*, 342–351. [[CrossRef](#)]
35. Duan, S.; Park, J. Comparison of Oxidation Behavior of Various Reactive Elements in Alloys during Electroslag Remelting (ESR) Process: An Overview. *ISIJ Int.* **2022**, *62*, 1561–1572. [[CrossRef](#)]
36. Zouvelou, N.; Mantzouris, X.; Nikolopoulos, P. Interfacial energies in oxide/liquid metal systems with limited solubility. *Int. J. Adhes. Adhes.* **2007**, *27*, 380–386. [[CrossRef](#)]

37. Li, J.; Cheng, G.; Ruan, Q.; Pan, J.; Chen, X. Formation and evolution of oxide inclusions in titanium-stabilized 18Cr stainless steel. *ISIJ Int.* **2018**, *58*, 2280–2287. [[CrossRef](#)]
38. Li, J.; Cheng, G.; Ruan, Q.; Pan, J.; Chen, X. Effect of CaO-MgO-SiO₂-Al₂O₃-TiO₂ slags with different CaF₂ contents on inclusions in Ti-stabilized 20Cr stainless steel. *ISIJ Int.* **2019**, *59*, 2013–2023. [[CrossRef](#)]

Disclaimer/Publisher’s Note: The statements, opinions and data contained in all publications are solely those of the individual author(s) and contributor(s) and not of MDPI and/or the editor(s). MDPI and/or the editor(s) disclaim responsibility for any injury to people or property resulting from any ideas, methods, instructions or products referred to in the content.